



## Cloud field segmentation via multiscale convexity analysis

Sin Liang Lim<sup>1</sup> and B. S. Daya Sagar<sup>2</sup>

Received 9 September 2007; revised 27 February 2008; accepted 31 March 2008; published 10 July 2008.

[1] Cloud fields retrieved from remotely sensed satellite data resemble functions depicting spectral values at each spatial position  $(x,y)$ . Segmenting such cloud fields through a simple thresholding technique may not provide any structurally significant information about each segmented category. An approach based on the use of multiscale convexity analysis to derive structurally significant regions from cloud fields is addressed in this paper. This analysis requires (1) the generation of cloud fields at coarser resolutions and (2) the construction of convex hulls of cloud fields, at corresponding resolutions by employing multiscale morphologic opening transformation and half-plane closings with certain logical operations. The three basic parameters required from these generated multiscale phenomena in order to accomplish the structure-based segmentation include (1) the areas of multiscale cloud fields, (2) the areas of corresponding convex hulls, and (3) the estimation of convexity measures at corresponding resolutions by employing the areas of cloud fields and areas of corresponding convex hulls. These convexity measures computed for multiscale cloud fields are plotted as a function of the resolution imposed owing to multiscale opening to derive a causal relationship. The scaling exponents derived from these graphical plots are taken as the basis for (1) determining the transition zones between the regimes and (2) segmenting the cloud fields into morphologically significant regions. We demonstrated this approach on two different cloud fields retrieved from Moderate Resolution Imaging Spectroradiometer (MODIS) data. The segmented regions from these cloud fields possess different degrees of spatial complexities. As many macroscale and microscale atmospheric fields are classified according to spatial variability indexes, the framework proposed here would supplement those existing atmospheric field classification methodologies.

**Citation:** Lim, S. L., and B. S. Daya Sagar (2008), Cloud field segmentation via multiscale convexity analysis, *J. Geophys. Res.*, *113*, D13208, doi:10.1029/2007JD009369.

### 1. Introduction

[2] Clouds are formed through the condensation and deposition of tiny water droplets and ice crystal and exist in various shapes and sizes. The understanding of clouds in spatial-temporal modes has greatly enhanced with the advent of satellite remote-sensing and computer-assisted mapping techniques. Many different macroscale and microscale atmospheric fields such as cloud top pressure, cloud fields, aerosol concentration, and cloud particle effective radius could be derived from remotely sensed data [e.g., Ackerman *et al.*, 1998, and references therein]. Lately, Moderate Resolution Imaging Spectroradiometer (MODIS) channels provide researchers with several different data of land, sea, and atmospheric fields, the characterization of which has received wide attention through seminal works [e.g., Inoue, 1987; Rossow, 1989; Gao and Goetz, 1991; King *et al.*, 1992, 1996; Hutchison and Hardy, 1995; Frey *et*

*al.*, 1995; Ackerman, 1997]. Several studies address the topic of the retrieval of zones from cloud fields possessing both naturally and anthropogenically generated aerosols with varied concentrations and from cloud particle effective radius maps via spatial variability tests.

[3] Geophysical fields such as landscapes, rainfall fields, cloud fields, and fields depicting various macroscale atmospheric fields are spatially heterogeneous to varied degrees. Such fields can be decomposed into threshold sets to facilitate characterization in planar forms. For a better characterization of geophysical fields, in recent decades several advanced procedures have been proposed and implemented efficiently. However, many of them are scale dependent. Scale-dependent parameters are inadequate to approximately characterize cloud field. After seminal works by Mandelbrot [1982] and several others, studies related to the characterization of geophysical fields via fractal analysis have been significantly refined. Fractal concepts and conventional morphometric analysis offer robust tools and techniques to characterize geophysical fields further to explore links with processes involved. The spatial complexities of some of such geophysical fields and/or sets are quantified [e.g., Rodriguez-Iturbe and Rinaldo, 1997; Sagar

<sup>1</sup>Faculty of Engineering and Technology, Multimedia University, Melaka, Malaysia.

<sup>2</sup>Indian Statistical Institute-Bangalore Centre, Bangalore, India.

and Tien, 2004; Sagar and Chockalingam, 2004; Tay et al., 2005, 2006, 2007].

[4] Atmospheric cloud is one of the important geophysical fields. A cloud can be treated as a surface of highly time dependent phenomenon. Segmentation of cloud fields is helpful for understanding in depth the cloud fields' characteristics. Spatial patterns exhibited by certain macroscale atmospheric fields (e.g., cloud fraction, cloud top pressure, cloud optical depth, column water vapor, and cloud particle effective radius) as observed from MODIS satellites are analyzed by Mote and Frey [2006]. Variations in spatial and spectral phenomena of clouds of various climatic zones are quantified via three leading principal components [Huang and Yung, 2005]. K-means cluster algorithm is used to classify satellite cloud scenes, over southern Great Plains acquired during the cool seas months between November and March 1999–2001, into distinct regions [Gordon et al., 2005]. Using three-dimensional (3-D) simulations of radiative transport and the independent pixel approximation (IPA), the characteristics of radiation transport in inhomogeneous clouds are studied [Zimmer et al., 2006].

[5] From a physical view, a cloud field is an aggregation of cloud ice, cloud water, and aerosols. All these parameters within a cloud make a cloud field possess brightness values distributed heterogeneously. If the brightness values of a cloud field are distributed homogeneously across all the spatial coordinates, simple thresholding technique is the choice for segmenting such a cloud field. However, the brightness values of realistic cloud fields are heterogeneously distributed. For segmenting cloud fields properly, simple thresholding techniques have the two following limitations: (1) in no way would morphologic constitution be considered, and (2) choice of threshold gray values is highly arbitrary.

[6] Shape-based segmentation of clouds has hitherto received little attention. In view of this, we opine that the segmentation of cloud into regions of morphologic significance would provide a new insight, which would be a step forward. Regions within a cloud can be classified/categorized according to their general morphological constitutions and furthermore could be linked according to their potential to yield precipitation.

[7] Characterization schemes include methods to derive properties of cloud surface roughness. Such schemes would be of use to quantify behaviors of time-dependent properties of cloud fields undergoing dynamic evolution. Segmentation based on structural and/or textural variations of clouds through multiscale convex analysis is addressed in this paper to derive zones of morphologic significance from a cloud field. We consider cloud fields retrieved from MODIS RGB color composites.

[8] We propose a procedure for segmentation of cloud field via multiscale morphological convexity analysis, which is popular in shape description analysis [e.g., Serra, 1982]. Stepwise procedures and the importance of each procedure are given as follows.

### 1.1. Generation of Cloud Fields and Convex Hulls at Multiple Scales

[9] Multiscale gray scale opening transformation is applied on a cloud field to generate coarsened versions of the

cloud field at 100 different resolutions, and computation of their corresponding convex hulls is done by employing half-plane closings. By performing increasing degrees of opening transformation, which is similar to generating a cloud field at coarser resolutions, one can observe the transition zones that demarcate the boundaries between the morphologic regimes at crossover scales.

### 1.2. Convexity Measures

[10] Areas of cloud fields and corresponding convex hulls across all the scales are used to estimate multiscale convexity measures. Convexity measure, in other words, cloud density, is defined as the ratio between the areas of the cloud field and its corresponding convex hull. This convexity measure is clearly resolution dependent, and it characterizes spatial heterogeneity of cloud fields. By assuming that the brightness values are distributed homogeneously within a cloud field, the convexity measures across all scales would be highly uniform. However, in a cloud field where brightness values are heterogeneously distributed, which is quite common in nature, the rates of change in the convexity measure differ significantly across scales. Hence, resolution-dependent convexity measures are estimated for a cloud field, to derive an appropriate basis to segment the cloud fields.

### 1.3. Determination of Morphologic Regimes

[11] Convexity measures are plotted as functions of scale parameter (i.e., radii of structuring element employed to generate multiscale clouds through opening transformation). This graphical relationship between convexity measure and scale parameter is taken as the basis for determining the transition zones between the two distinct, successive morphologic regimes. For a better understanding, a set and a schematic cloud field and their corresponding convex hulls are illustrated in Figures 1a–1f with an explanation in section 2 along with cloud data specifications. The cloud fields observed at transition zones (or) at crossover scales are further employed to segment the cloud field into morphologically significant zones.

[12] We note that this geometric approach can be applied directly on the gray level image, instead of the general method where the image has to be first transformed into two colors, black and white only. Hence, loss of information in the binarization process of the input function can be avoided. This multiscale convexity analysis based cloud segmentation depends on gray values' arrangement rather than on gray values' ranges. This procedure is stable and can be generalized to segment the cloud fields irrespective of the dynamic ranges of gray values. This convexity analysis based segmentation procedure provides results that are independent of spatial and spectral resolutions as regimes between the crossover scales do not change significantly with changes in spatial and/or spectral resolutions.

[13] This paper includes MODIS cloud data specifications (section 2), basic morphological transformations needed to develop a framework (section 3), generation of cloud field at multiple resolutions and the convex hull estimation using half-plane closing (section 4), area estimation of a gray scale image and its corresponding convex hull (section 5), empirical relationships between various

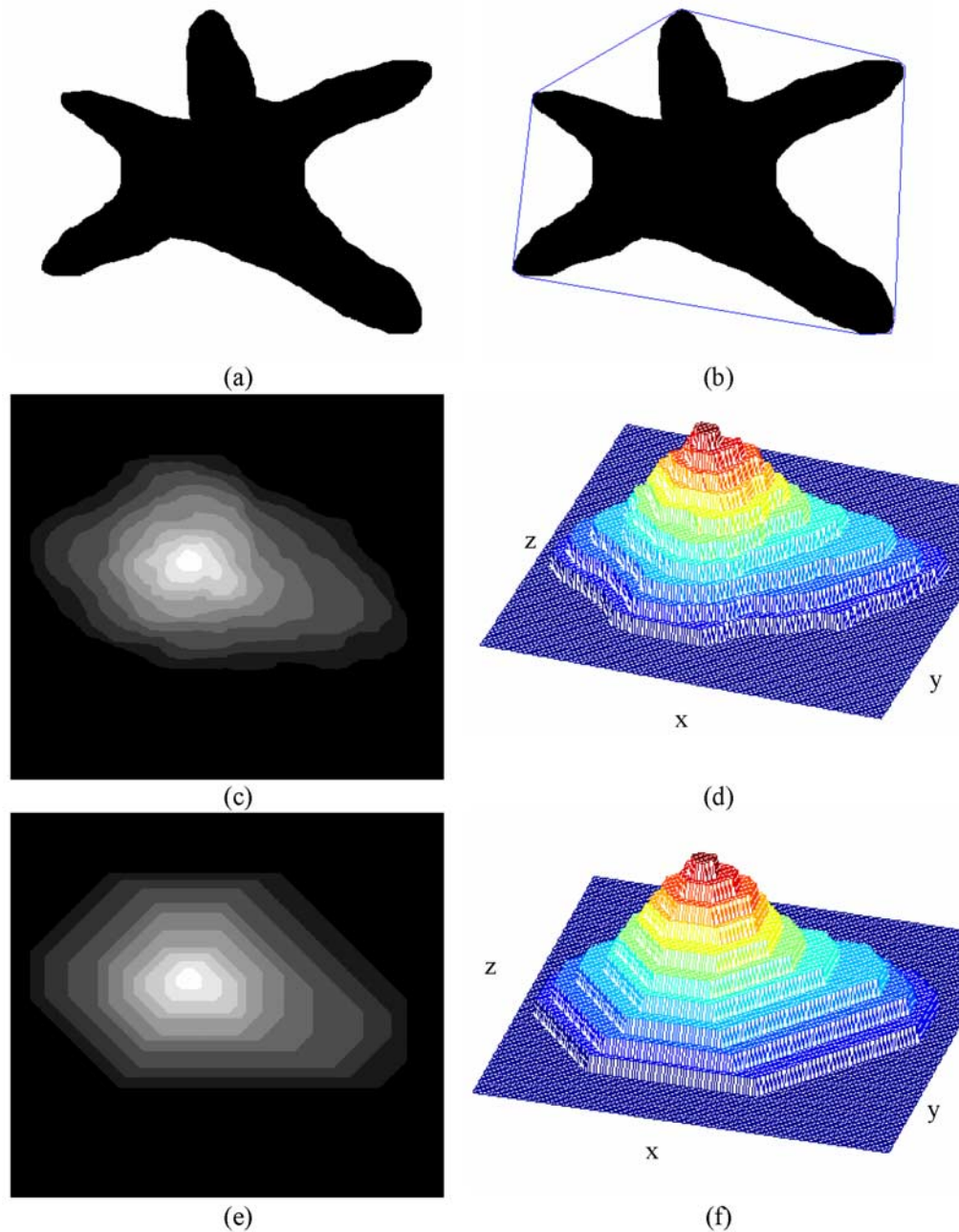


**Figure 1.** (a) A threshold set decomposed from a synthetic cloud function, (b) convex hull of a threshold set shown in Figure 1a, (c) a synthetic cloud function consisting of 10 gray levels, which can be decomposed maximally into 10 threshold sets, (d) 3-D representation of synthetic cloud function, shown in Figure 1c, where  $x, y$  depict spatial coordinates and  $z$  represents corresponding gray levels at respective  $x, y$  spatial coordinates, (e) convex hull of synthetic cloud function shown in Figure 1c, and (f) 3-D representation of convex hull shown in Figure 1e.

parameters and discussion (section 6), and concluding remarks (section 7).

## 2. Data Used and Their Specifications

[14] Moderate Resolution Imaging Spectroradiometer (MODIS) data are the ideal data source for resource and environmental remote-sensing monitoring on the regional scale [Song *et al.*, 2004]. We consider two cloud images

(Figures 2a and 2c), belonging to regions situated between the spatial coordinates  $60^{\circ}$ – $74^{\circ}$ E,  $20^{\circ}$ – $28^{\circ}$ N and  $150^{\circ}$ – $162^{\circ}$ W,  $2^{\circ}$ – $10.5^{\circ}$ N, respectively, acquired through MODIS (<http://modis-atmos.gsfc.nasa.gov/IMAGES/index.html>). Figure 2a was acquired on 30 June 2006 (Day 181) at 1510 UTC with a size of  $851 \times 621$  pixels, while Figure 2c was obtained on 28 May 2007 at 2355 UTC with a size of  $797 \times 512$  pixels. The original images are in true color (bands 1, 4, and 3 for red, green, and blue channels,

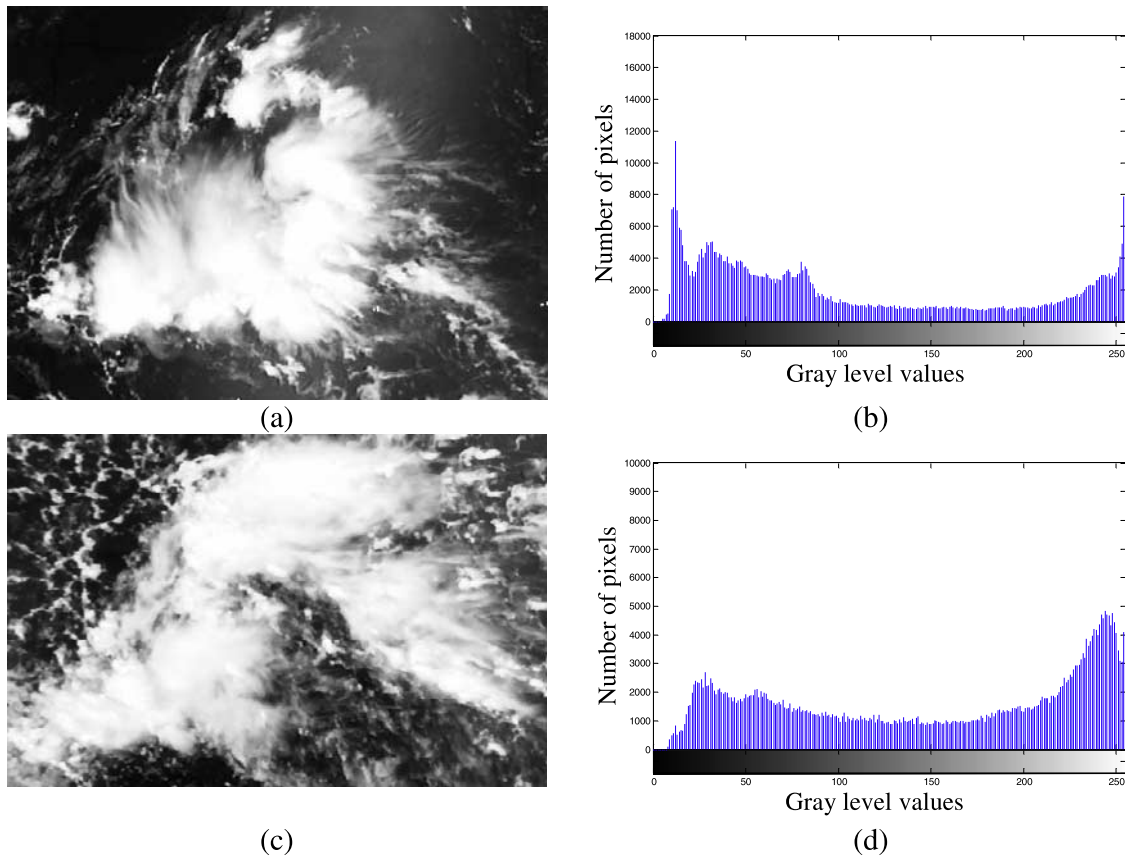


**Figure 2.** (a) Isolated Moderate Resolution Imaging Spectroradiometer (MODIS) cloud (cloud-1), (b) histogram of Figure 2a, (c) isolated MODIS cloud (cloud-2), and (d) histogram of Figure 2c. Refer to text for the spatial and time details of clouds acquired by MODIS satellites.

respectively). The images are then converted to gray scale functions  $f(x,y)$  (multilevel signals) with 8 bits/pixel. Thus the values for  $f(x,y)$  vary from 0 to 255, with value 0 representing black and value 255 representing pure white (an ideal case); values in between 0 and 255 (i.e., 1–256) denote shades of gray which range sequentially from dark gray to lighter gray shades. A true color image is a 24-bit image consisting of 8-bit images, for red (R), green (G), and blue (B) planes, respectively. As processing of a 24-bit image is computationally highly expensive, a 24-bit true color image is converted into a 8-bit gray scale image. Processing a 8-bit image is straightforward and is acceptable in remotely sensed data analysis studies. The corresponding histograms of Figures 2a and 2c are shown in Figures 2b and 2d, respectively. It is observed that most of the pixel values are distributed either toward dark gray to black or toward light gray to white, with a peak value at 255 (white) in Figure 2b. This can be explained from Figure 2a such that a large patch of seemingly thick white cloud constitutes the middle of the image.

[15] Convex hull construction for both threshold set and function is illustrated in Figure 1. Figures 1a and 1c depict the synthetic forms of threshold cloud set and cloud function, respectively. Typical convex hulls of threshold set and cloud function are shown in Figures 1b and 1e, respectively. It is obvious that a starfish-like set (Figure 1a) possesses a polygon-like convex hull (Figure 1b). It is also

evident that the convex hulls act as supersets of their corresponding input information. In turn, the areas of convex hulls are greater than or equal to their corresponding functions (sets). In the synthetic cloud function (Figure 1c), it is conspicuous that there are 10 gray levels, and such a function can be decomposed into a maximum of ten threshold sets. Such decomposed sets possess their boundaries in rather contorted forms. In the convex hulls of such function, it can be seen that the decomposed threshold sets possess smooth boundaries maintaining convexities. The function-like image and its convex hull (Figures 1c and 1e) are also represented in 3-D forms (Figures 1d and 1f). The construction of convex hulls is mathematically explained in later sections.

### 3. Methodology

[16] In this section, we briefly discuss (1) basic gray scale morphological transformations, (2) half-plane closing, and (3) convex hull construction.

#### 3.1. Basic Morphological Transformations

[17] Mathematical morphology [Serra, 1982] is originally based on set theory, where sets represent objects in an image. The sets (or binary images) in question are represented as white (or black, depending on convention) pixels at the  $(x,y)$  coordinates in the image, defined in 2-D discrete

(a) Morphological Erosion of $f$ by $B$														
19	25	21	30	25	18	0	.	.	.	.	.	.	.	
14	17	16	222	20	15	1	.	12	16	16	15	1	.	
8	12	240	254	208	10	3	.	8	12	208	10	3	.	
9	209	250	255	254	200	7	.	9	209	250	200	7	.	
15	208	240	253	252	195	8	.	9	195	232	9	4	.	
2	9	195	232	9	4	2	.	2	8	7	4	2	.	
0	5	8	7	6	5	4	.	.	.	.	.	.	.	
$f$							$\ominus$	$B$	=	$f \ominus B$				
(b) Morphological Dilation of $f$ by $B$														
19	25	21	30	25	18	0	.	25	240	254	222	20	.	
14	17	16	222	20	15	1	.	240	254	255	254	208	.	
8	12	240	254	208	10	3	.	250	255	255	255	254	.	
9	209	250	255	254	200	7	.	240	253	255	254	252	.	
15	208	240	253	252	195	8	.	208	240	253	252	195	.	
2	9	195	232	9	4	2	.	.	.	.	.	.	.	
0	5	8	7	6	5	4	.	.	.	.	.	.	.	
$f$							$\oplus$	$B$	=	$f \oplus B$				
(c) Morphological Opening of $f$ by $B$														
19	25	21	30	25	18	0	.	16	16	208	16	15	.	
14	17	16	222	20	15	1	.	12	209	250	208	10	.	
8	12	240	254	208	10	3	.	209	250	250	250	200	.	
9	209	250	255	254	200	7	.	195	232	250	232	9	.	
15	208	240	253	252	195	8	.	9	195	232	9	4	.	
2	9	195	232	9	4	2	.	.	.	.	.	.	.	
0	5	8	7	6	5	4	.	.	.	.	.	.	.	
$f$							$\circ$	$B$	=	$(f \ominus B) \oplus B = f \circ B$				

**Figure 3.** (a–c) Basic gray scale morphological transformations, where  $\ominus$ ,  $\oplus$ , and  $\circ$  denote morphologic erosion, dilation, and opening, respectively. Erosion, dilation, and opening of a function of size  $7 \times 7$  transformed by means of a flat structuring element of size  $3 \times 3$  that is symmetric about origin and rhombic in shape.

space  $Z^2$ . Mathematical morphology deals with transforming sets or functions according to certain transformation rules with reference to a probing rule, also called structuring element. Basic morphologic transformations considered in this investigation include erosion, dilation, opening, and closing [Serra, 1982]. Morphological operations can also be extended to a gray scale image, which is represented as a function [Sternberg, 1986; Maragos, 1989]. Here, at the  $(x, y)$  coordinates of a pixel, it is assigned a value corresponding to its associated discrete gray level value,  $f(x, y)$ . In this paper, we focus on application of gray scale morphological transformations rather than on applying binary morphologic transformations. Hence, we avoid explaining binary morphologic transformations.

[18] Gray level image  $f(x, y)$ , an array containing digital values at each  $(x, y)$  spatial coordinate, is defined as a finite subset in  $Z^2$ . The range of these values depends on the bit/pixel that is considered. For the following discussion, we deal with the digital image (function) of the form  $f(x, y)$  and structuring element  $B$ . Structuring element  $B$  considered is flat, rhombic in shape, symmetric about origin, and of primitive size  $3 \times 3$  (e.g., Figures 3a–3c). Gray scale morphological dilation and erosion transformations are defined, respectively, as

$$(f \oplus B)(x, y) = \max_{(i, j) \in B} \{f(x - i, y - j)\}, \quad (1)$$

$$(f \ominus B)(x, y) = \min_{(i, j) \in B} \{f(x + i, y + j)\}, \quad (2)$$

where  $\oplus$  and  $\ominus$  denote dilation and erosion, respectively. Erosion transformation replaces the central values of neighborhood images with the minimum gray values within the neighborhood; whereas dilation transformation replaces the central values within the neighborhood image by the maximum value within the neighborhood. Hence, these two transformations are dual to each other, as long as the sizes of the neighborhood images are the same. Erosion makes the image darkened, while dilation makes the image brightened. The dilation (erosion) transformation of  $f$  by  $B$  (a primitive, flat, symmetric structuring element) computes maxima (minima) in function by moving  $B$  across the function (e.g., Figures 3a–3c). These two transformations are explained illustratively in Figures 3a and 3b. From equations (1) and (2), it is obvious that erosion is the duality of dilation, because eroding the foreground pixels is equivalent to dilating the background pixels [Serra, 1982]. Dilation expands an object in question, while erosion shrinks the object. The two possible combinations of dilation and erosion operations result in opening and closing operations, which are used for smoothing purposes. Opening of  $f$  by  $B$  is achieved by first eroding  $f$  and then dilating the result with  $B$ . Closing is the reverse of opening, where dilation of  $f$  by  $B$  is performed first, followed by erosion with respect to  $B$ . These two nonlinear morphological transformations are as follows:

$$(f \circ B) = [(f \ominus B) \oplus B], \quad (3)$$

$$(f \bullet B) = [(f \oplus B) \ominus B], \quad (4)$$

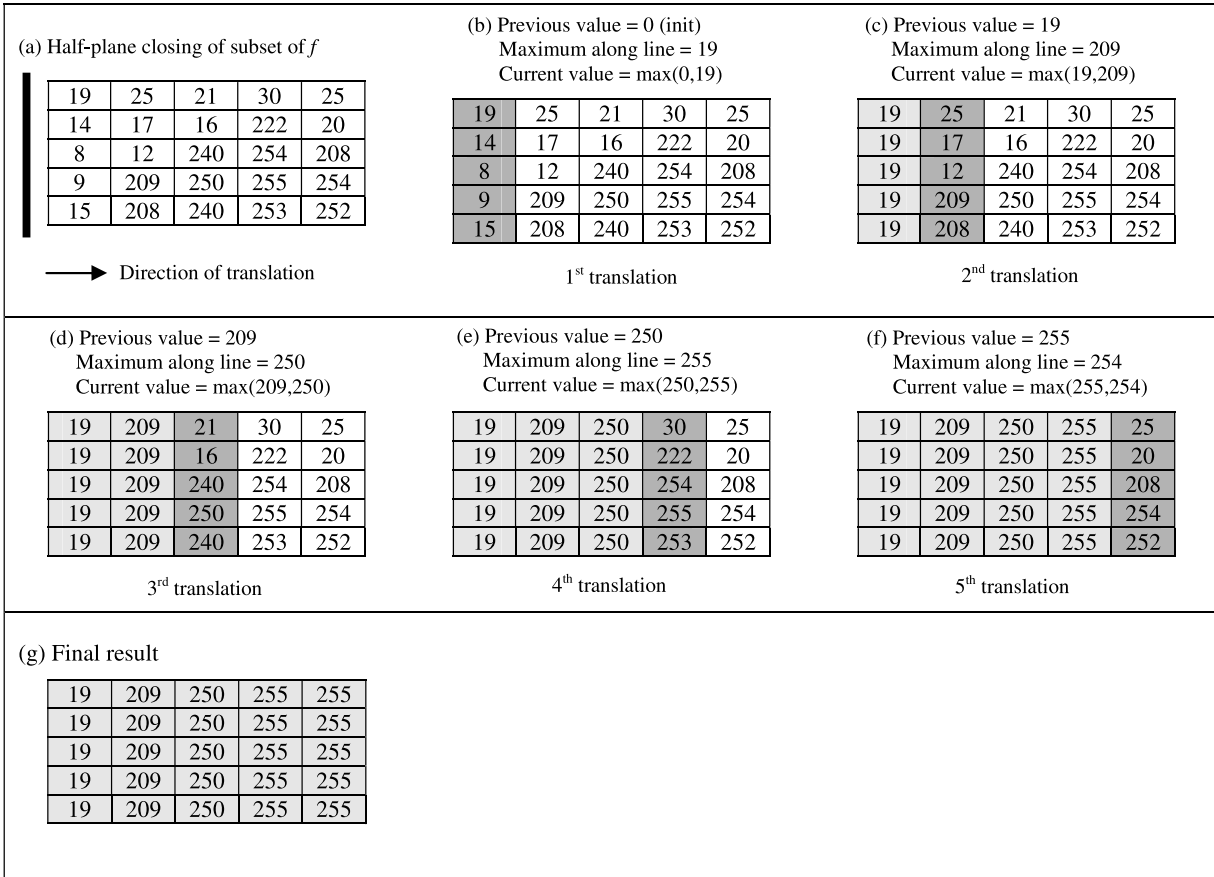


**Figure 4.** (a–f) Sequential steps involved in obtaining successive five translations (Figures 4b–4f) of a function of size  $5 \times 5$  shown in Figure 4a, via left-vertical half plane to achieve half-plane closing of the function, and (g) half-plane closing obtained by left-vertical half plane of a function shown in Figure 4a.

where  $\circ$  and  $\bullet$  denote opening and closing, respectively. Opening (e.g., Figure 3c) tends to eliminate particular image details smaller than  $B$ ; thus it is able to remove noise and smooth the boundaries from the inside, while closing fills holes in objects, connects small breaks, and smoothes the boundaries from the outside. Furthermore, we employ these transformations (equations (3) and (4)), to generate a function at multiple scales, where the size (scale) characteristic will be imposed on  $B$  as  $(B \oplus B \oplus B \dots \oplus B = n^{\text{th}} \text{ size of } B)$ , as multiscale opening and closing at scale  $n = 0, 1, 2, \dots$ . These multiscale transformations are as follows:

$$(f \circ nB) = [(f \ominus nB) \oplus nB], \tag{5}$$

$$(f \bullet nB) = [(f \oplus nB) \ominus nB]. \tag{6}$$

Multiscale opening of scale  $n$  is expressed as erosion of image  $f$  by  $B$  for  $n$  number of times followed by dilation with the same  $B$  for  $n$  times. In contrast, multiscale closing of scale  $n$  is defined as dilation of  $f$  by  $B$  for  $n$  times followed by erosion with  $B$  for  $n$  times. In this work, closings by several half planes are required essentially to construct convex hull of the function. With closing (either half-plane closing or general closing to obtain convex hull), holes within a cloud would be filled, small breaks would be

connected, and overall the complex cloud field would be converted into a rather smooth cloud field. To explain this further, closing of a complex cloud field generates a rather smoothed version of cloud field. The degree of smoothing depends upon the size of structuring element considered to perform closing. In order to convert an image that is spatially heterogeneous into spatially rather homogeneous, in other words convex, we need to perform a transformation to construct convex hull of the image. By constructing a convex hull, one needs to make sure that holes are filled, small breaks are connected, and boundaries are smoothed.

### 3.2. Half-Plane Closing

[19] Half-plane closing by left-vertical half plane is explained in Figures 4a–4g. Figure 4a is a subimage of the synthetic image shown in Figure 3a. The reason for choosing this subimage is to explain the half-plane closing with fewer translations. To transform a function via closing by left-vertical half plane (shown as a dark line) in the forward direction, half plane is moved to the first column of the function. Each gray value in that column coinciding with the half plane is evaluated to find out the maximum values. The first translation involved replacing all the values in that column with a maximum value if such a value is not less than the value in the previous translation. This is a recursive process until the last column in that direction.

Once all the columns of the function in left-right direction are translated via left-vertical half plane, it is called closing of function by left-vertical half plane and is denoted by  $[\phi_{\pi_{\theta}^+}(f)]$ . Similarly, by considering right-vertical half plane in the direction right to left from the rightmost column, the values are translated until the leftmost column to generate closing function by right-vertical half plane. This process is known as closing of function by right-vertical half plane, denoted by  $[\phi_{\pi_{\theta}^-}(f)]$ . In a similar fashion, closings of the function by other half planes are generated by changing the directions. For better comprehension, in section 3.3, we show the process of generating closings by half planes of eight directions on a function represented in an array of size  $7 \times 7$ . Figures 4a–4f and 5a–5r further explain the construction of a convex hull.

### 3.3. Convex Hull Construction via Half-Plane Closing

[20] Convex hull of a grayscale cloud field is defined as threshold superposed smallest convex sets of all possible threshold sets or level sets [e.g., *Sethian*, 1999] that could be decomposed from a cloud field. A threshold set is convex if and only if the line segment connecting any two pairs of points of the set is included in the set [*Zunic and Rosin*, 2004]. The gray scale convex hull of a synthetic cloud field (Figure 1c) represented in gray scale form is illustrated in Figure 1e. Convex hull of a cloud field can also be constructed directly by computing the point-wise minimum  $\Lambda$  between the closings obtained by half planes in all possible directions (e.g., Figures 5j–5q). This can be done to avoid computing the convex hulls of threshold sets decomposed from a cloud field. Construction of the convex hull of a gray scale image, which is due to *Soille* [1998], is explained in the information that follows.

[21] A convex hull is defined as the smallest convex polygon containing all points in the set. It can be thought of as being obtained by using a rubber band; extending it outside all points and then letting it shrink [*Wennmyr*, 1989]. Construction of a convex hull of a set is a well-established procedure. However, to construct a convex hull of a function (e.g., cloud), we adopt the approach proposed by *Soille* [1998]. This construction requires two steps: (1) transformation of a function via closings by using half planes of all directions and (2) computation of point-wise minimum  $\Lambda$  between all versions of half-plane closings. This two-step process of convex hull ( $CH(f)$ ) construction is as follows:

$$CH(f) = \Lambda_{\theta} \left[ \phi_{\pi_{\theta}^+}(f) \Lambda \phi_{\pi_{\theta}^-}(f) \right], \quad (7)$$

where  $(\pi_{\theta}^+)^c = \pi_{\theta}^-$  denotes two half planes at orientation  $\theta$  and  $\phi(f)$  represents the closing of a gray scale image  $f$ . For better comprehension, we demonstrate this two-step approach to generate convex hull by considering a synthetic discrete cloud function of size  $7 \times 7$  (Figure 3a). Figures 5a–5h illustrate the half planes of eight different directions with a function. These eight directions include vertical half planes of right and left sides, horizontal half planes of lower and upper sides, and also diagonal half planes of top left, bottom right, top right, and bottom left sides. Figures 5j–5q show closings of  $f$  obtained by eight different half planes shown in Figures 5a–5h, respectively. Figures 5j–5m show half-plane closing by left-right vertical

planes and upper-lower horizontal planes, accordingly. Figures 5n–5q represent the closings of another two pairs of orientation, namely  $\frac{3\pi}{4}$  and  $\frac{\pi}{4}$ . The maximum value of the column before the first column is considered as zero. By performing the point-wise minimum ( $\Lambda$ ) among the eight half-plane closing versions (Figures 5j–5q), the convex hull is computed (Figure 5r). Note that the precision of the computed convex hull increases with the number of directions and converges to the real convex hull of the image, at the expense of higher complexity and greater computation time [*Soille*, 1998].

## 4. Multiscale Cloud Fields and Their Convex Hulls

[22] A cloud field is an aggregation of various subimages (cloud subfields). These subfields have different sizes and shapes. Increasing degree of multiscale can be performed to filter out subfields of increasing sizes. This section deals with (1) generation of cloud at multiscales using morphologic opening and (2) construction of a convex hull of cloud by using half-plane closing.

### 4.1. Multiscale Cloud Generation

[23] In order to generate cloud function at multiple resolutions and to construct their corresponding convex hulls, morphological opening (equation (5)) is used. The cloud fields  $f$  (Figures 2a and 2c) under the influence of an increasing degree of opening are progressively flattened, mimicking the generation of cloud fields at coarser resolutions. Higher degrees of opening transformation change cloud field in such a way that the cloud field gets disconnected before the entire cloud function vanishes. Figure 6 illustrates selected levels of cloud function transformed via multiscale opening. Furthermore, in order to investigate the multiscale property of MODIS cloud field, we generate 100 “opened” images using multiscale opening operations, on the basis of equation (5). The scale factor  $n$  will vary from 1 to 100. Note that the opened image  $f$  with  $n = 0$  is the same as  $f$ . The structuring element  $B$  has the shape of a disc and is bounded, convex, symmetric, and contains the origin. For viewing the 100 pairs of “opened” images and their corresponding convex hulls, refer to Figure S1 in the auxiliary material.<sup>1</sup> We show that the cloud field evolving via opening transformation possesses initial and boundary conditions. These boundary conditions include flattened cloud and the convex hull of cloud field, respectively. In order to quantify the cloud field’s morphological changes, we choose to parameterize the cloud, evolving morphologically owing to multiscale opening, with convexity measures.

### 4.2. Construction of Convex Hulls

[24] By following the approach explained on a synthetic function (section 3.3), the convex hull of a MODIS cloud image (Figure 2a) is constructed (Figure 7i). Figure 2a is the input gray scale image, while Figures 7a–7h depict the closings computed using eight directional half planes. Figures 7a–7d show closings of  $f$  by left-right vertical planes and upper-lower horizontal planes, accordingly.

<sup>1</sup>Auxiliary materials are available in the HTML. doi:10.1029/2007JD009369.



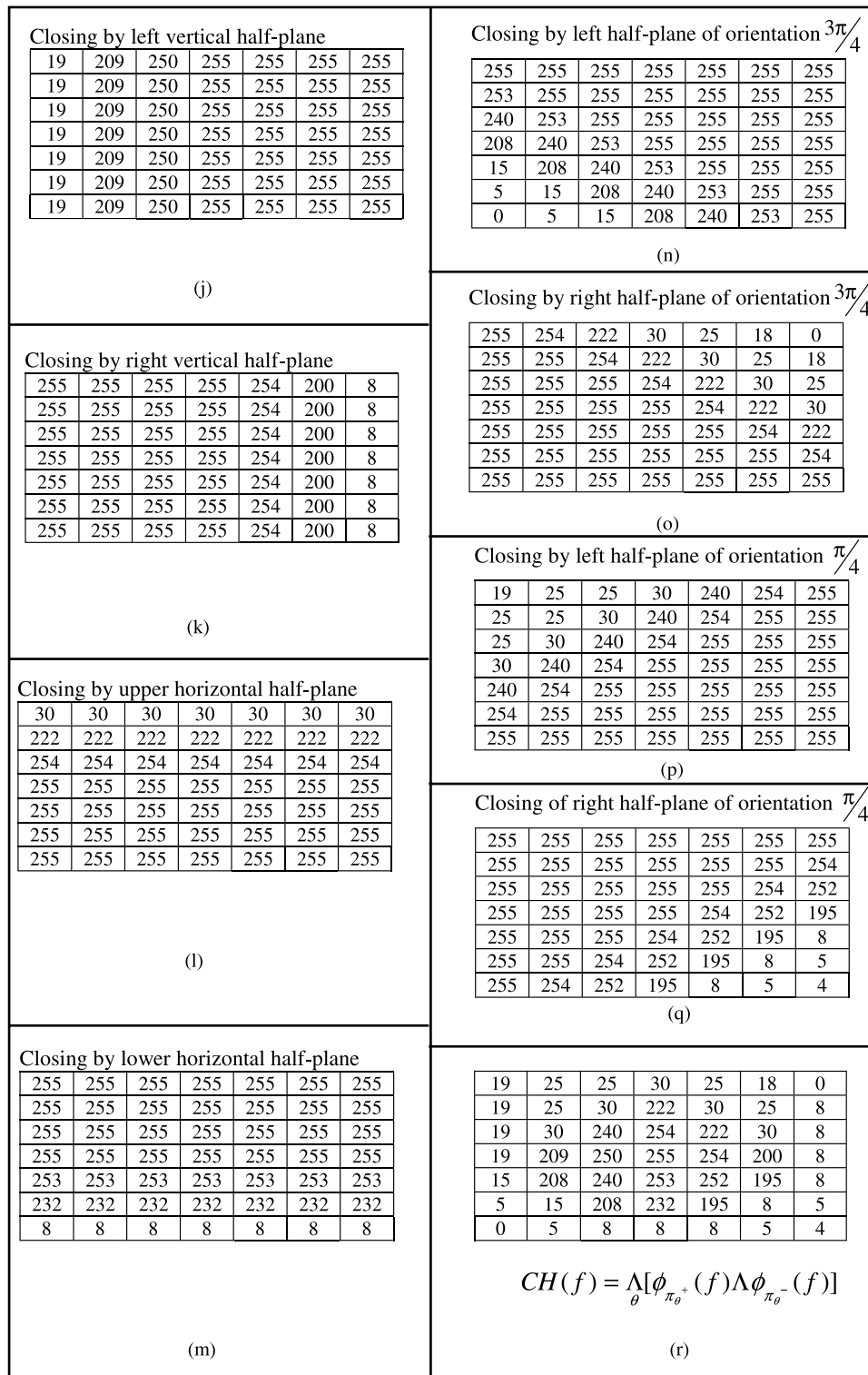
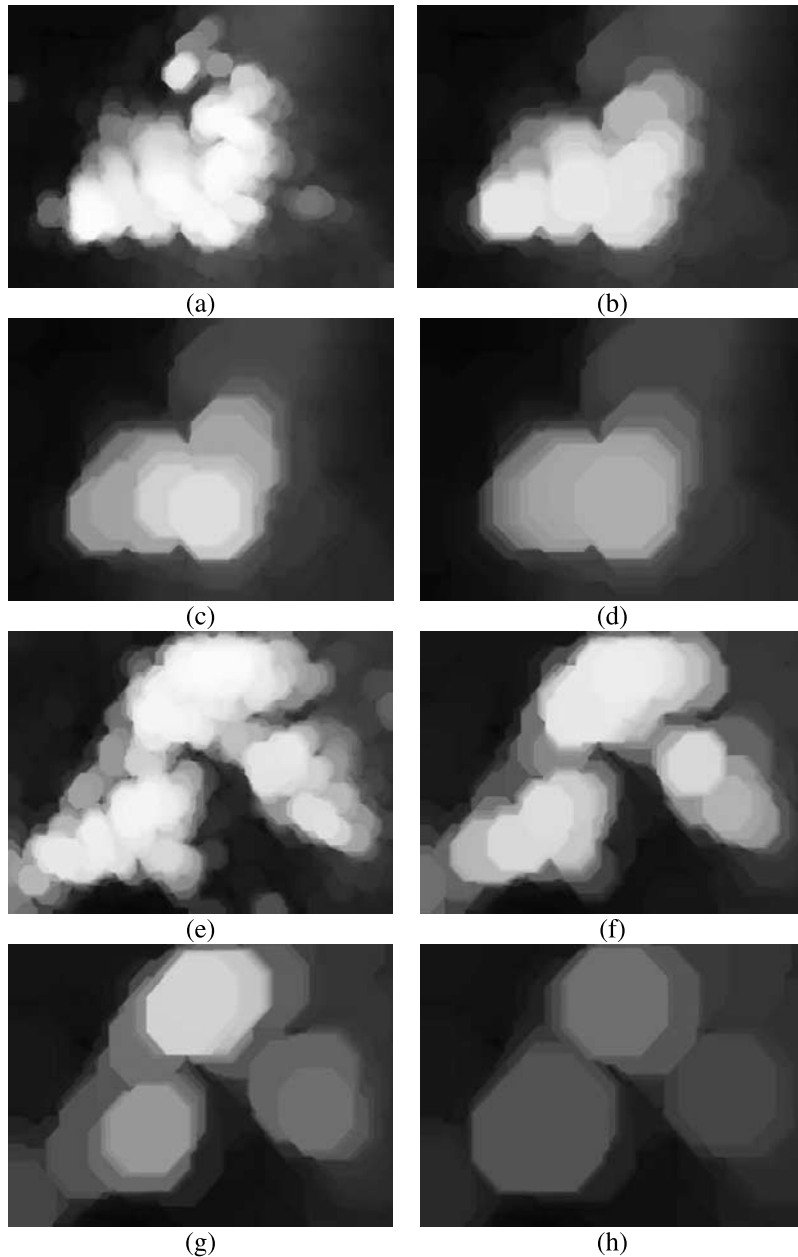


Figure 5. (continued)

Figures 7e–7h present the closings of another two pairs of orientation, namely  $\frac{3\pi}{4}$  and  $\frac{\pi}{4}$ . Finally, the point-wise minima of Figures 7a–7h result in the gray scale convex hull (Figure 7i). We note that eight directions are considered in the computation of Figure 7i. In fact, the same number of directions is used in the construction of all convex hulls of

corresponding multiscale cloud images with the approach described above. In Figures 8a–8d and Figures 8e–8h, we selectively show the gray scale convex hull obtained for the 25th, 50th, 75th, and 100th opened MODIS cloud images shown in Figures 6a–6h, respectively. It is observed that the



**Figure 6.** (a–d) Images of 25 cycles, 50 cycles, 75 cycles, and 100 cycles, respectively, of opened versions of cloud function shown in Figure 2a. (e–h) Images of 25 cycles, 50 cycles, 75 cycles, and 100 cycles, respectively, of opened versions of cloud function shown in Figure 2c. Refer to Figure S1 for all the opened versions ranging from 1 to 100.

convex hull decreases in size and encompasses smaller cloud area as the size of structuring element  $B$  increases.

### 5. Estimation of Area of Multiscale Clouds and Their Convex Hulls and Convexity Measure

[25] In section 4, cloud functions are generated at multiple scales by performing multiscale opening transformation. The convex hulls of corresponding multiscale cloud functions are constructed. A cloud field possesses a convex hull that acts as a super set to cloud field, and hence the area of the convex hull is greater than or equal to its corresponding cloud field. Area estimation of clouds at multiple scales and

their corresponding convex hulls, so as to compute the convexity measure, is briefly explained in this section. The area of cloud function (and also convex hull function) is the area computed as the sum of the gray values corresponding to the pixels of all spatial positions within a function. Mathematically, the computation of the area is

$$A(f) = \sum_{(x,y)} f(x,y) \quad \text{and} \quad A[CH(f)] = \sum_{(x,y)} CH[f(x,y)]. \quad (8)$$

It is obvious that the areas of multiscale cloud fields at decreasing resolution, together with areas of their corre-

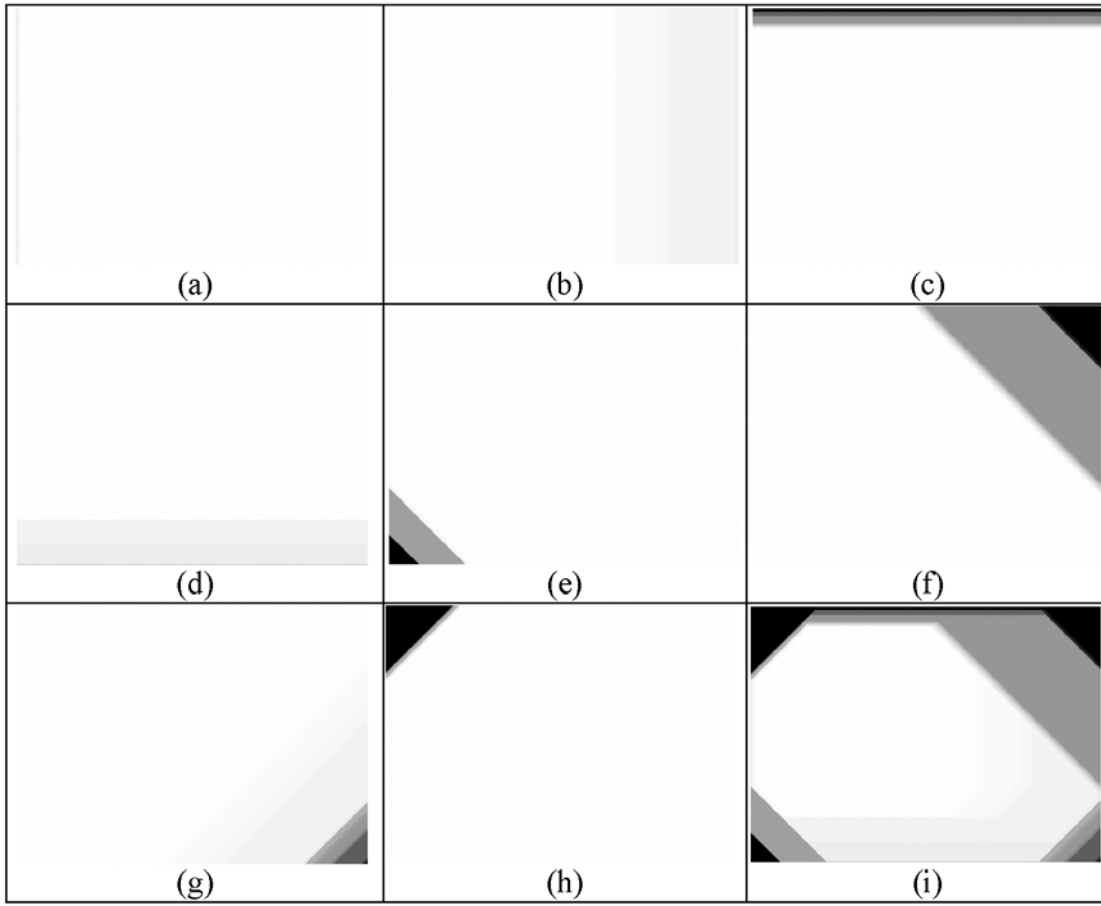


**Figure 7.** Convex hull generation of cloud function (Figure 2a) by half planes, based on the work of Soille [1998]: (a) left-vertical half plane, (b) right-vertical half plane, (c) upper horizontal half plane, (d) lower horizontal half plane, (e) left half plane of orientation  $\frac{3\pi}{4}$ , (f) right half plane of orientation  $\frac{3\pi}{4}$ , (g) right half plane of orientation  $\frac{\pi}{4}$ , (h) left half plane of orientation  $\frac{\pi}{4}$ , and (i) intersection of all half-plane closings from Figures 7a–7h, resulting in gray scale convex hull of cloud function shown in Figure 2a. It should be noted that Figures 7a, 7b, 7d, and 7h contain thin gray or black streaks on left, right, bottom, and top left sides of the panels, respectively.

sponding convex hulls at decreasing resolutions, are in a decreasing trend (Figures 9a and 9b). These relationships are mathematically expressed as (1)  $A(f) \geq A(f \circ 1B) \geq A(f \circ 2B) \geq \dots \geq A(f \circ (N-1)B) \geq A(f \circ NB)$ , (2)  $A[CH(f)] \geq A[CH(f \circ 1B)] \geq A[CH(f \circ 2B)] \geq \dots \geq A[CH(f \circ (N-1)B)] \geq A[CH(f \circ NB)]$ , and (3)  $A(f \circ nB) \leq A[CH(f \circ nB)]$ ,  $n = 0, 1, 2, \dots, N$ .

[26] To determine the lost area (probability) distribution (across the scales to understand the general trend) of MODIS cloud surface and its convex hull, we employ equations (9a) and (9b). Equations (9a) and (9b) enable the computation of probability distribution values [e.g., Maragos, 1989] for original cloud  $p_f(r, B)$  and its convex hull  $p_{CH(f)}(r, B)$ , respectively:

$$p_f(r, B) = \frac{A(\text{for}B) - A(f \circ (r+1)B)}{A(f)}, 0 \leq r \leq N, \quad (9a)$$

$$p_{CH(f)}(r, B) = \frac{A[CH(\text{for}B)] - A[CH(f \circ (r+1)B)]}{A[CH(f)]}, 0 \leq r \leq N, \quad (9b)$$

where  $A(f)$  and  $A(\text{for}B)$  represent the areas of original cloud function and the cloud function opened in terms of scale parameter denoted by radius  $r$  of  $B$ :  $A[CH(f)]$  and  $A[CH(\text{for}B)]$  denote the areas of convex hull function of original cloud function and the convex hull areas of cloud functions opened by structuring elements of different radii. Under the influence of opening transformation successively implemented by increasing the size  $r$  of  $B$ , the image ( $f$  and in turn  $CH(f)$ ) tends to lose its area with increasing  $r$  of  $B$ . We know that the total area of the image is  $A(f)$ . The portion of area that is lost at the opening level by  $rB$  from  $A(f)$  and in turn from  $A[CH(f)]$  will be reflected in equations (9a) and (9b) and Figures 9e and 9f. The probability distribution values computed through equations (9a) and (9b) satisfy the following relationships: (1)  $0 \leq (p_f(r, B), p_{CH(f)}(r, B)) \leq 1$ , (2)  $\sum_{r=0}^N p_f(r, B) = 1$ , and (3)  $\sum_{r=0}^N p_{CH(f)}(r, B) = 1$ .

[27] Clouds are neither flat like sheets nor spherical like balls for adequately quantifying the degree of regularity. In fact, their dimensions are more than sheets but less than spheres. However, their corresponding convex hulls are

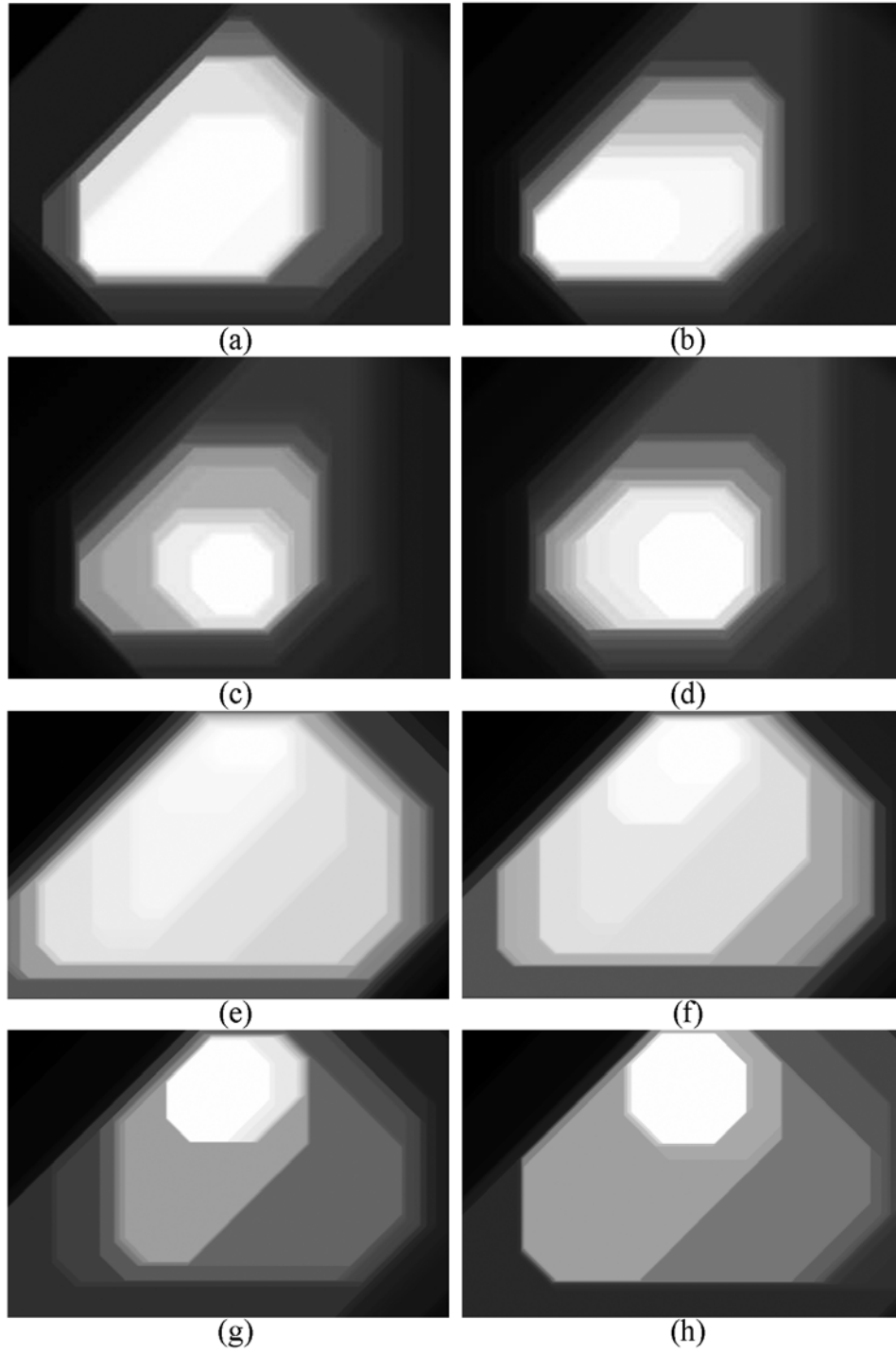


**Figure 8.** (a–d) Convex hulls of 25th, 50th, 75th, and 100th opened versions of cloud-1 and (e–h) convex hulls of 25th, 50th, 75th, and 100th opened versions of cloud-2. For convex hulls of opened versions at all resolutions, generated from cycle 1 to 100, refer to Figure S2 in the auxiliary material.

rather regular in geometry. For the characterization of clouds of varied spatial heterogeneities, we consider the ratio between cloud area and its convex hull area, which could range between  $(0, 1)$  as the area of a convex hull of a cloud is always greater than or equal to the area of its cloud; hence this ratio (equation (10)) can never exceed the unity value. We define multiscale convexity measure  $CM_{\text{for } B}$

as the ratio of areas under the function  $A_{\text{for } B}$  and its corresponding convex hull  $A[CH_{\text{for } B}]$ :

$$CM_{\text{for } B} = \frac{A_{\text{for } B}}{A[CH_{\text{for } B}]} \quad (10)$$

The convexity measure 1 of a cloud is valid if and only if the areas of the cloud and its convex hull are the same (e.g.,

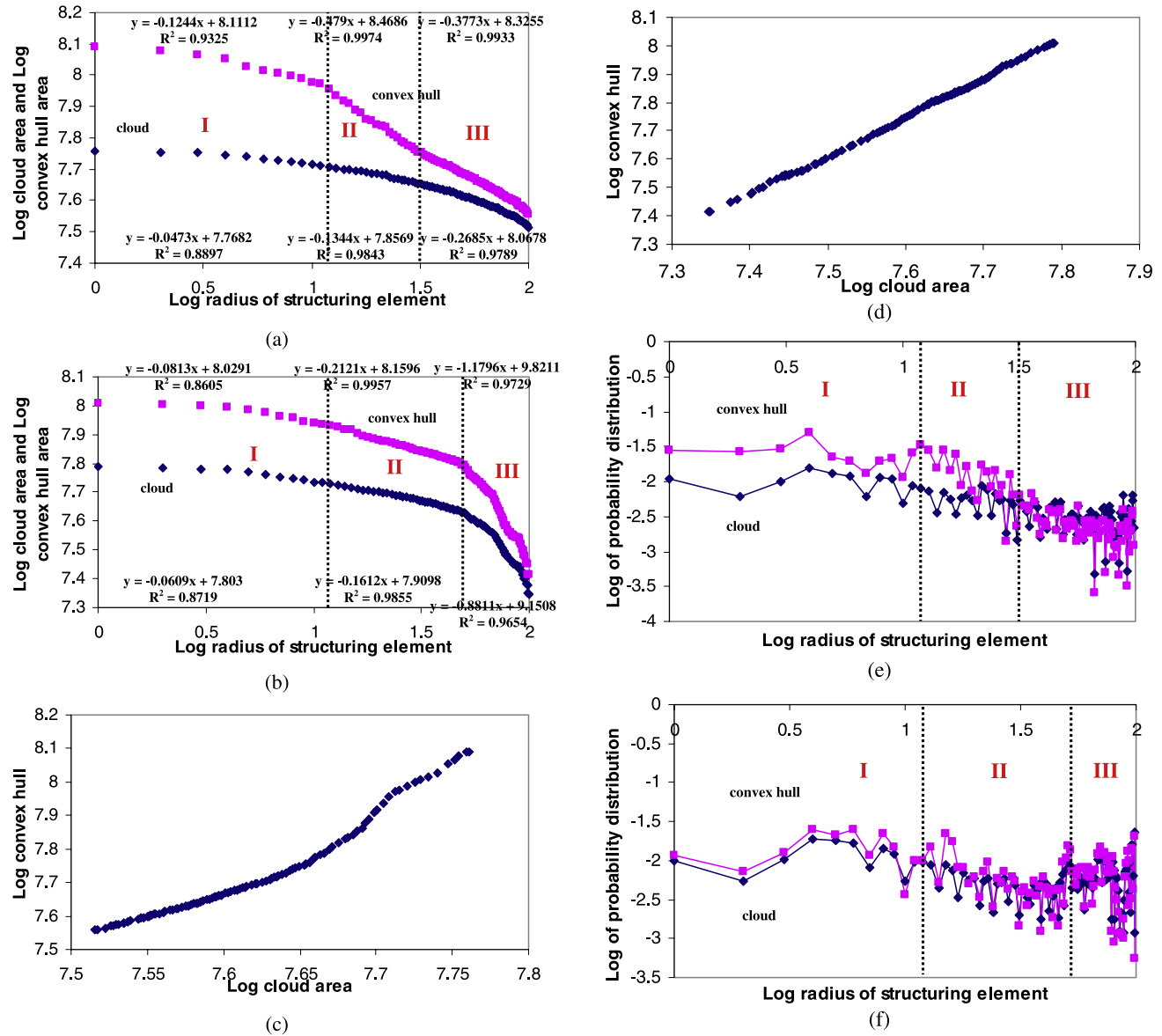


**Figure 9.** (a) Log-log graph between cloud area and convex hull versus corresponding radius of structuring element for cloud-1. (b) Log-log graph between cloud area and convex hull versus corresponding radius of structuring element for cloud-2. (c) Log-log graph of convex hull versus cloud area for cloud-1. (d) Log-log graph of convex hull versus cloud area for cloud-2. (e) Log-log graph between the radii of structuring templates and corresponding probability distribution values for cloud-1. (f) Log-log graph between the radii of structuring templates and corresponding probability distribution values for cloud-2. (g) Log-log graph between convexity measure with increasing radius of structuring element for cloud-1. (h) Log-log graph between convexity measure with increasing radius of structuring element for cloud-2.

flat and spherical clouds, as their convex hulls are also respectively flat and spherical; under such circumstances, the areas of such a cloud and its convex hull are equal to one another). When there are too many perforations in a so-called connected irregular cloud, then the area of the convex hull of such a cloud would be much larger than the area of such a perforated cloud, and its convexity measure will be close to zero. The cloud surface can be covered with a blanket-like convex hull, construction of which is explained in section 4.2, denoted by  $CH\{f(x,y)\}$ . The area under such a function is also estimated according to equation (8).

[28] Since we are interested in exploring the multiscale property of a MODIS cloud field, we decrease the resolution of Figures 2a and 2c by varying the size of the structuring element  $B$  from 1 to 100. As we perform multiscale opening with an increasing degree of opening by means of increasing the size of  $B$ , the process of generating a function at coarser resolutions is mimicked. Increasing the degree of multiscale opening converts an image into smoothed versions. The higher the degree of multiscale opening, the higher the degree of smoothing. Hence, we obtain cloud images at decreasing resolutions with an increasing degree of

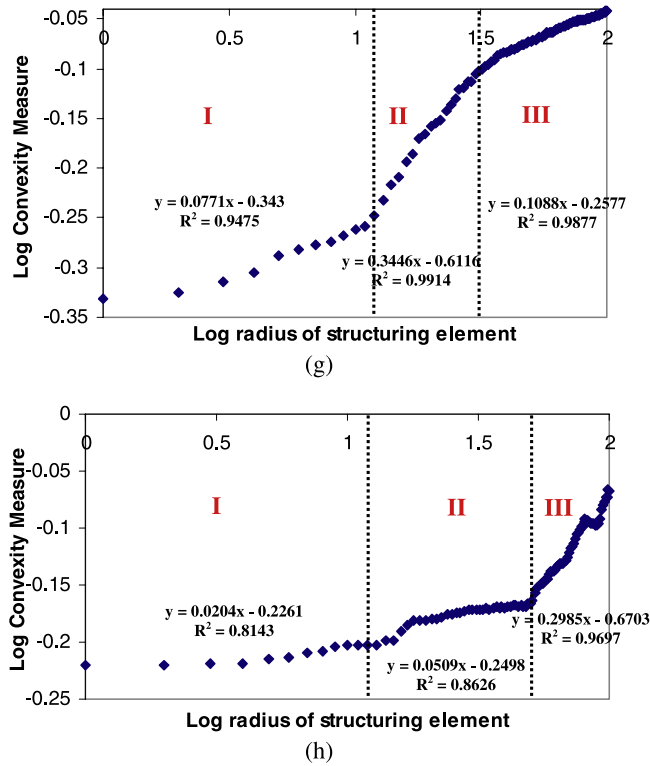


Figure 9. (continued)

multiscale opening. Specific degrees of multiscale openings of the clouds (Figures 2a and 2c) are shown in Figures 6a–6d and 6e–6h, respectively. The areas for the “opened” image and its corresponding convex hull are computed, according to equation (8). Probability size distribution values are estimated for both multiscale clouds and their corresponding convex hulls according to equations (9a) and (9b). Loss of information, estimated in terms of area change across scales simulated by means of multiscale opening transformation, is considered to estimate the probability size distribution functions for both multiscale cloud function and corresponding convex hull functions. The relationship between convexity measure and size of structuring element  $B$  for both considered cloud fields is shown in section 6 along with a discussion.

### 6. Relationships Between the Areas and Multiscale Degree, Scale, and Convexity Measure Across Scales: Results and Discussion

[29] Empirical relationships between the areas and multiscale degree, scale and probability values, and scale and convexity measures are addressed in this section. The two cloud fields (Figures 2a and 2c), their multiscale clouds generated via 100 cycles of opening (Figure S1), and their corresponding convex hulls (Figure S2) generated through approaches explained in sections 4.1 and 4.2 are considered for sequential analysis to obtain the morphologic regimes to appropriately segment the cloud fields. To achieve appropriate segmentation process, changes that occur across multiscale cloud fields and their corresponding convex hulls are recorded in terms of areas. The areas of multiscale

clouds and their corresponding convex hulls are plotted as functions of scale, which is imposed owing to structuring element size on a logarithmic scale (Figures 9a and 9b). It is obvious that the areas of cloud fields and their convex hulls at decreasing resolutions are in decreasing trend. The rate at which the areas are getting reduced with increasing opening cycles is less in the cloud than in its convex hull. It is also observed that the areas of multiscale clouds and their corresponding convex hulls are merging at a point (Figures 9a and 9b). It is obvious from Figures 9a and 9b that the multiscale clouds are the subfunctions of corresponding convex hulls as the areas of the clouds at respective scales are always less than their corresponding convex hulls’ areas. Figures 9a and 9b also explain the difference between the cloud fields and their corresponding convex hulls in terms of areas that are gradually decreasing with increasing cycle of opening. At the coarser resolution of cloud, the degree of variation between the areas of coarser cloud (cloud after largest cycle of opening) and its convex hull is minimal. This further supports the fact that the convexity measure is in increasing trend with increasing cycle of opening. The larger the cloud area, the larger is its convex hull area. To further support these statements, we show the relationship between the areas of the convex hull and its cloud on a log-log scale (Figures 9c and 9d). For both cloud-1 and cloud-2, according to this graphical relationship, the areas of cloud and its convex hull are more or less similar where the area of cloud function is minimal (less). However, the areas of convex hulls at finer resolutions, at which the cloud function obviously possesses more area, are significantly more than that of the corresponding cloud function. More or less linear relationships are observed from these plots, further supporting that the larger the area of cloud field, the larger its convex hull area.

[30] The log-log graph is plotted for both probability values of multiscale cloud fields and their convex hulls as functions of scale parameter  $r$  (radius of structuring element) (Figures 9e and 9f). The probability distribution values for a convex hull are always greater than that of cloud at all scales. Similar trends are observed in the plots for both cloud and convex hull, further supporting the fact that these two features are geometrically interdependent. Similar trends in variations in the probability distribution values between the cloud and convex hull are observed in all three regimes marked on Figures 9e and 9f. These graphs also exhibit that loss of information in cloud and convex hull across scales is, in general, in decreasing trend. In other words, greater information is lost as the radius of the structuring element increases.

[31] We conjecture that the  $\alpha$  exponent that can be observed from  $CM(f) \sim [r]^\alpha$  relationship varies with spatial complexity of cloud fields. In this relationship,  $r$  is a structuring element with radius  $r$  ranges between 1 to  $N$ , and  $\alpha$  is a piece-wise power law. We hypothesize that this exponent varies with spatial complexity of cloud function. Convexity measure is locally scale invariant. There are three regimes observed that are locally scale invariant. Through the relationships between (1) radius of structuring element and probability distribution values for both cloud fields and corresponding convex hulls (Figures 9a, 9b, and 9e–9h) and (2) radius of structuring element and areas of multiscale

clouds and their convex hulls, we observed that there exist three different morphological regimes. The crossover scales/radii are observed, for cloud-1, at scales or radii of structuring element of 1, 12, 32, and 100, where 1 and 100 are lower and upper limits.

[32] The basis to properly classify the topological region of a cloud field appears valid in terms of the relationship between scale factor ( $r$ ) and convexity measure relationships (Figures 9g and 9h). In the middle region of the cloud-1 (Figure 2a) (i.e., 12th cycle of opening to 32nd cycle of opening), the rate of change in convexity measure across resolutions is observed more than that of inner and external portions of cloud field. It is observed from Figures 9g and 9h that the convexity measure does not possess a universal power law exponent with respect to increasing radius of structuring element. As a basis to categorize the cloud field, the convexity measure pattern across scales is thus divided into three groups (Figures 9g and 9h). We classify Group I as the convexity measure corresponding to structuring element from  $n = 1$  to 11, Group II as the convexity measure extracted with structuring element from  $n = 12$  to 31, and finally Group III as the remaining convexity measure computed relative to structuring element from  $n = 32$  to 100. Nevertheless, all groups exhibit an increasing trend with increasing size of structuring element. In Group I, the graph shows a rather flat curve, with a slope value of only 0.0771. This indicates that the rate of increment in convexity measures is slow at a smaller radius of structuring element. When we increase the radius of structuring element from 12 to 31, we obtain a steeper curve with slope value of 0.3446. This means that convexity measure obtained within this region shows a high rate of change, as compared to Groups I and III. Owing to logarithmic representation, the convexity measures for the structuring element between  $n = 32$  and 100 are shown to be “squeezed” in Group III, as seen in Figure 9g. Even though the graph seems to be saturated and approaching a specific value, it actually yields a gradient value of 0.1088. Hence, we can conclude that in terms of convexity measure, Group II exhibits a higher rate of change, followed by Group III showing a moderate rate of change, and lastly Group I giving the slowest rate of increment, across multiple resolutions. For cloud-2, a similar graphical relationship is shown in Figure 9h. The analysis of this graph provides three morphologic regimes in the structuring elements’ size ranges:  $n = 1-11$  (Group I),  $n = 12-48$  (Group II), and  $n = 49-100$  (Group III), respectively. The rates of change in the convexity measure across these groups include 0.0204, 0.0509, and 0.2985, respectively. When convexity measure is plotted as a function of scale factor (structuring element size), the graphical relationships have not shown any linear trend. On the basis of the graphs, we regrouped the cloud field under morphological evolution into three groups based on the local slopes (Figures 9g and 9h). Locally, these convexity measures exhibit scale-invariant properties, although their global trends have not shown any scale-invariance property. These findings further facilitate a way to segment the cloud regions into zones of morphologic significance. These segmented zones can be better linked with various macroscale atmospheric fields.

[33] To have a view of information loss in cloud field across multiple resolutions, we generated Figures 10a and

10c on the basis of the segregated phases shown in Figures 9g and 9h. We note from Figure 9g that the graph of convexity measures of opened versions of cloud-1 shows a sudden change at radii 12 and 32 (crossover scales), for Group II and Group III, respectively. The cloud images at the 12th cycle, 32nd cycle, and 100th cycle of opening are converted into binary images by choosing a common threshold value. These threshold cloud images are superposed on one another after coding them with colors for better visualization (Figure 10a). The boundaries of these threshold cloud images are superposed on the original cloud-1 (Figure 2a) for better viewing, and it is observed that the regions embedded within the segmented zones have different degrees of spatial homogeneities (Figure 10b). These classes for cloud-1 and cloud-2 are separated by choosing an “opening level” of image that changes abruptly, which can be observed from the graphs (Figures 9g and 9h). The first abrupt change in cloud-2 as depicted from Figure 9h is at opening level 12 (i.e., when  $r = 12$ ), and the second abrupt change could be seen at opening level 49; as we terminated the iteration of opening at 100th cycle, we choose opening level 100 as the third threshold opening level. The images obtained by opening levels 12, 49, and 100 are thresholded by choosing gray value 110. For better clarity, these thresholded images are color-coded by blue, gray, and red, respectively. These color-coded segmented regions are superposed on the thresholded original image, which is color-coded with green. In fact, this green zone is the remainder of the cloud after subtracting the three classes segmented and represented with blue, gray, and red zones. Superposing the zones (with blue, gray, and red) on the thresholded original image (depicted with green) yields Figure 10c. Hence, effectively there are four segmented zones. This entire process is true to the results shown for the four zones (Figures 10a and 10c) for cloud-1 and cloud-2, respectively. The boundaries of these four segmented zones are also superposed on the original cloud-1 and cloud-2 (Figures 10b and 10d).

## 7. Conclusion

[34] This paper provides a framework for segmenting cloud fields on the basis of multiscale convexity analysis. The criterion to choose multiple regimes is based on the transition zones that can be observed from the graphs plotted between the radius of structuring element and the convexity measure. To retrieve the morphologic regions, we visualized cloud field at multiple resolutions, via multiscale morphologic opening. Estimation of convexity measures at respective scales is done by computing the ratio between the areas of cloud field and its corresponding convex hull. Prior to area estimation, we perform multiscale morphological opening to transform cloud fields retrieved from MODIS product at multiple scales. Furthermore, convex hulls of these multiscale cloud fields are constructed by following half-plane closing approaches. This analysis provides a way to classify cloud field into regions of prominence in a quantitative manner. From the results, it is observed that the segmented regions follow a pattern from a smooth/compact interior to a rough/broken boundary. This objective method of smoothing and shrinking the cloud field into a sequence of embedded regions (sorted by area) is non-

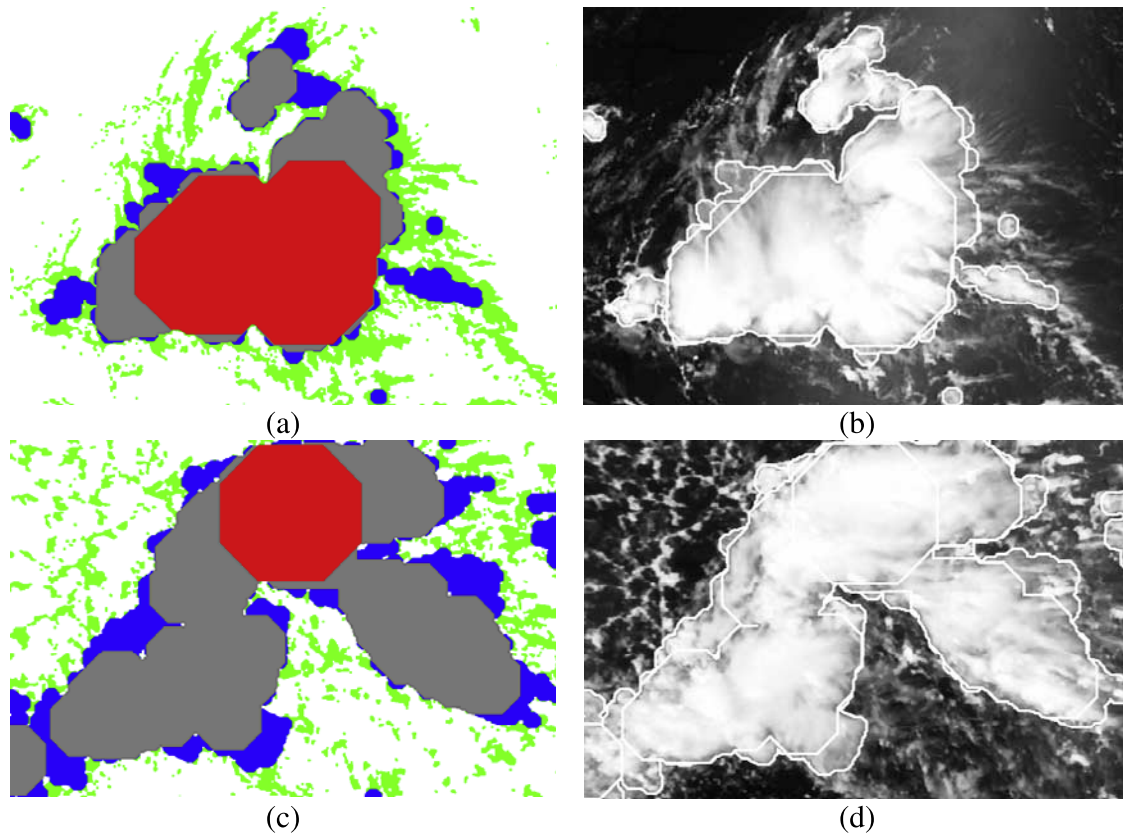


**Figure 10.** (a) Color-coded binarized (by choosing threshold gray level value 128) cloud-1 images at three threshold-opening cycles superimposed on binarized original cloud-1 color-coded with green, (b) boundaries of 12th, 32nd, and 100th opened cloud-1 images and thresholded original cloud-1 superimposed on the original cloud image, (c) color-coded binarized (by choosing threshold gray level value 110) cloud-2 images at threshold-opening cycles superimposed on binarized original cloud-2 color-coded with green, and (d) boundaries of 12th, 49th, and 100th opened cloud-2 images and thresholded original cloud-2 superimposed on the original cloud image. Different regions, which are categorized broadly as inner (red), middle (gray), and two outer (blue and green) regions, depict zones with different spatial heterogeneities.

trivially related to pixel brightness. Through a multiscale convexity analysis-based approach to segment cloud fields, one cannot expect the same statistical robustness from simple thresholding on brightness at the pixel scale. The approach followed in this study complements the scale-based methods of quantifying cloud surfaces.

[35] It is shown that through convexity measure of the cloud, segmentation of the cloud into prominent regions can be performed. The segmented regions with different convexity characteristics quantified numerically may be properly related to the region-wise physically retrieved measurements of aerosol, cloud particle effective radius, and several other parameters that could be derived from macroscale and microscale atmospheric fields.

[36] Overall, this paper addresses the problem of segmenting cloud fields retrieved from remotely sensed data. The approach used in this paper is based on computing convex hulls of multiscale cloud field by using mathematical morphology and deriving a multiscale convexity measure. This approach is inherently multiscale, which is consistent with the turbulent nature of clouds and of many other atmospheric phenomena. The main finding in this

paper is that, on the basis of the inspection of some key scaling relations established between scale and multiscale convexity measures, the two real-world cloud fields are segmented into three distinct regimes. The number of regimes depends on the shape-size complexity of cloud. The higher the number of crossover scales, the higher the number of regimes that one can segment. Crossover scales depend on both shape and size complexities of the cloud.

[37] Most of the approach can be automatized except the determination of crossover scales/structuring element radii to delineate different regimes, from radii and convexity measure relationship. The derivation of threshold opening levels depends on the proper determination of crossover scales from a log-log graph of convexity measure ( $CM$ ) and scale ( $r$ ). At this stage, crossover scales' determination is done interactively. However, this proposed approach has the second limitation. As a whole, this new approach mitigates the first limitation. It would be interesting to explore the algorithms to automatically derive the crossover scales from the graphs depicted for  $CM$  and  $r$ . Within each segmented zone (e.g., within each of three regimes segmented), if one uses different threshold values instead of just value 128,

which is chosen arbitrarily here for cloud-1, one can see subclassification within each segmented zone. Through such subclassification, perhaps one can distinguish the open cell convection (e.g., at the top left corner of cloud-2 from the more closed-cell-like convection at the bottom right corner).

[38] Further, this approach can be used to assess the realism/validity of cloud models by comparison between simulated and real data. It would be worth applying this new multiscale analysis tool to synthetic data (e.g., fractal shapes and multifractal fields) with known multiscale properties for calibration purpose. Some results obtained through the application of multiscale analysis, which is essentially based on binary morphologic transformations, can be seen at <http://www1.mmu.edu.my/~sllim2/>. Application of structure-based segmentation would be useful to partition the cloud field that consists of cloud ice—cloud water that possesses different morphologic characteristics. The approach proposed here (1) groups cloud even in quite chaotic scenes according to horizontal size of cloud structures (e.g., convective cells) and (2) can be foreseen in cloud classification to identify different cloud types.

[39] **Acknowledgments.** The authors are highly grateful to the three anonymous reviewers for providing useful comments and suggestions that strengthened the manuscript.

## References

- Ackerman, S. A. (1997), Remote sensing aerosols from satellite infrared observations, *J. Geophys. Res.*, *102*, 17,069–17,079.
- Ackerman, S. A., K. I. Strabala, W. P. Menzel, R. A. Frey, C. C. Moeller, and L. E. Gumley (1998), Discriminating clear sky from clouds with MODIS, *J. Geophys. Res.*, *103*, 32,141–32,157.
- Frey, R. A., S. A. Ackerman, and B. J. Soden (1995), Climate parameters from satellite spectral measurements, I. Collocated AVHRR and HIRS/2 observations of the spectral greenhouse parameter, *J. Clim.*, *9*, 327–344.
- Gao, B. C., and A. F. H. Goetz (1991), Cloud area determination from AVIRIS data using water vapor channels near 1  $\mu\text{m}$ , *J. Geophys. Res.*, *96*, 2857–2864.
- Gordon, N. D., J. R. Norris, C. P. Weaver, and S. A. Klein (2005), Cluster analysis of cloud regimes and characteristic dynamics of midlatitude synoptic systems in observations and a model, *J. Geophys. Res.*, *110*, D15S17, doi:10.1029/2004JD005027.
- Huang, X. L., and Y. L. Yung (2005), Spatial and spectral variability of the outgoing thermal IR spectra from AIRS: A case study of July 2003, *J. Geophys. Res.*, *110*, D12102, doi:10.1029/2004JD005530.
- Hutchison, K. D., and K. R. Hardy (1995), Threshold functions for automated cloud analyses of global meteorological satellite imagery, *Int. J. Remote Sens.*, *16*, 3665–3680.
- Inoue, T. (1987), A cloud type classification with NOAA 7 split window measurements, *J. Geophys. Res.*, *92*, 3991–4000.
- King, M. D., Y. J. Kaufman, W. P. Menzel, and D. Tanre (1992), Remote sensing of cloud, aerosol, and water vapor properties from the Moderate Resolution Imaging Spectrometer (MODIS), *IEEE Trans. Geosci. Remote Sens.*, *30*, 2–27.
- King, M. D., et al. (1996), Airborne scanning spectrometer for remote sensing of cloud, aerosol, water vapor and surface properties, *J. Atmos. Oceanic Technol.*, *13*, 777–794.
- Mandelbrot, B. (1982), *The Fractal Geometry of Nature*, W. H. Freeman, San Francisco, Calif.
- Maragos, P. A. (1989), Pattern spectrum and multiscale shape representation, *IEEE Trans. Pattern Anal. Mach. Intel.*, *11*(7), 701–716.
- Mote, P. W., and R. Frey (2006), Variability of clouds and water vapor in low latitudes: View from Moderate Resolution Imaging Spectroradiometer (MODIS), *J. Geophys. Res.*, *111*, D16101, doi:10.1029/2005JD006791.
- Rodriguez-Iturbe, I., and A. Rinaldo (1997), *Fractal River Basins: Chance and Self-Organization*, Cambridge Univ. Press, New York.
- Rosow, W. B. (1989), Measuring cloud properties from space: A review, *J. Clim.*, *2*(3), 201–213.
- Sagar, B. S. D., and L. Chockalingam (2004), Fractal dimension of non-network space of a catchment basin, *Geophys. Res. Lett.*, *31*, L12502, doi:10.1029/2004GL019749.
- Sagar, B. S. D., and T. L. Tien (2004), Allometric power-law relationships of Hortonian fractal digital elevation model, *Geophys. Res. Lett.*, *31*, L06501, doi:10.1029/2003GL019093.
- Serra, J. (1982), *Mathematical Morphology and Image Analysis*, Academic, San Diego, Calif.
- Sethian, J. A. (1999), *Level Set Methods and Fast Marching Methods: Evolving Interfaces in Computational Geometry, Fluid Mechanics, Computer Vision and Materials Science*, Cambridge Univ. Press, New York.
- Soille, P. (1998), Grey scale convex hulls: Definition, implementation and applications, in *Proceedings of the Fourth International Symposium on Mathematical Morphology and Its Applications to Image and Signal Processing, Amsterdam, the Netherlands*, pp. 83–90, Springer, New York.
- Song, X., Z. Liu, and Y. Zhao (2004), Cloud detection and analysis of MODIS image, *Proc. IEEE IGARSS'04*, *4*, 2764–2767, doi:10.1109/IGARSS.2004.1369875.
- Stemberg, S. R. (1986), Greyscale morphology, *Comput. Vision Graphics Image Process*, *35*, 333–355.
- Tay, L. T., B. S. D. Sagar, and H. T. Chuah (2005), Analysis of geophysical network derived from multiscale digital elevation models: A morphological approach, *IEEE Trans. Geosci. Remote Sens. Lett.*, *2*(4), 399–403.
- Tay, L. T., B. S. D. Sagar, and H. T. Chuah (2006), Allometric relationships between travel-time channel networks, convex hulls, and convexity measures, *Water Resour. Res.*, *46*, W06502, doi:10.1029/2005WR004092.
- Tay, L. T., B. S. D. Sagar, and H. T. Chuah (2007), Granulometric analysis of basin-wise DEMs: A comparative study, *Int. J. Remote Sens.*, *28*(15), 3363–3378.
- Wenmyr, E. (1989), A convex hull algorithm for neural networks, *IEEE Trans. Circuits Syst.*, *36*(11), 1478–1484, doi:10.1109/31.41308.
- Zinner, T., B. Mayer, and M. Schroder (2006), Determination of three-dimensional cloud structures from high-resolution radiance data, *J. Geophys. Res.*, *111*, D08204, doi:10.1029/2005JD006062.
- Zunic, J., and P. L. Rosin (2004), A new convexity measure for polygons, *IEEE Trans. Pattern Anal. Mach. Intel.*, *26*(7), 923–934.

B. S. Daya Sagar, Indian Statistical Institute-Bangalore Centre, 8th Mile, Mysore Road, R. V. College (P.O.), Bangalore 560059, India. (bsdsagar@isibang.ac.in)

S. L. Lim, Faculty of Engineering and Technology, Multimedia University, Melaka Campus, Jalan Ayer Keroh Lama, 75450 Melaka, Malaysia. (lim.sin.liang@mmu.edu.my)